NeuroImage 47 (2009) 1261–1267

Contents lists available at ScienceDirect

NeuroImage

journal homepage: www.elsevier.com/locate/ynimg

In vivo mapping of the human locus coeruleus

Noam I. Keren [a,*], Carl T. Lozar [a], Kelly C. Harris [a], Paul S. Morgan [b,c], Mark A. Eckert [a]

[a] Department of Otolaryngology – Head and Neck Surgery, Medical University of South Carolina, 135 Rutledge Avenue, MSC550, Charleston, SC 29425, USA
[b] Department of Radiology and Radiological Science, Medical University of South Carolina, Charleston, SC, USA
[c] Division of Academic Radiology, University of Nottingham, Nottingham, UK

ARTICLE INFO

Article history:
Received 8 December 2008
Revised 29 May 2009
Accepted 2 June 2009
Available online 11 June 2009

ABSTRACT

The locus coeruleus (LC) is a brainstem structure that has widespread cortical and sub-cortical projections to modulate states of attention. Our understanding of the LC's role in both normal attention and clinical populations affected by disrupted attention would be advanced by having *in vivo* functional and structural markers of the human LC. Evidence for LC activation can be difficult to interpret because of uncertainty about whether brainstem activity can be accurately localized to the LC. High resolution T1-turbo spin echo (T1-TSE) magnetic resonance imaging (MRI) (in-plane resolution of 0.4 mm × 0.4 mm) was used in this study to characterize the location and distribution probability of the LC across 44 adults ranging in age from 19 to 79 years. Utilizing a study-specific brainstem template, the individual brainstems were aligned into standard space, while preserving variations in LC signal intensity. Elevated T1-TSE signal was observed in the rostral pons that was strongly correlated with the position and concentration of LC cells previously reported in a study of post-mortem brains ($r = 0.90$). The elevated T1-TSE signal was used to produce a probabilistic map of the LC in standard Montreal Neurological Institute (MNI) coordinate space. This map can be used to test hypotheses about the LC in human structural and functional imaging studies. Such efforts will contribute to our understanding of attention systems in normal and clinical populations.

Introduction

A large body of work has described cortical networks that support different dimensions of attention (see Posner, 2004) and there is a growing interest in the modulation of these cortical attention networks by brainstem nuclei (Aston-Jones et al., 2000; Bouret and Sara, 2005; Corbetta et al., 2008; Coull et al., 1999; D'Ardenne et al., 2008; Mohanty et al., 2008; Shea-Brown et al., 2008; Usher et al., 1999). The locus coeruleus (LC), which exhibits extensive projections with cortical and sub-cortical regions (Morecraft et al., 1992; Morrison and Foote, 1986; Morrison et al., 1982; Porrino and Goldman-Rakic, 1982), has been implicated in modulating attentional states (Aston-Jones et al., 2000). Progress testing hypotheses regarding the role of the human LC in attention has been slowed however, by technical limitations related to differentiating brainstem nuclei on MRI.

The LC is located adjacent to the floor of the fourth ventricle in the rostral pons and extends into the midbrain to the level of the inferior colliculi (Chan-Palay and Asan, 1989b; German et al., 1988; Manaye et al., 1995). LC cells are most densely populated at the level of the trochlear nucleus (Chan-Palay and Asan, 1989b; German et al., 1988; Manaye et al., 1995), however, there is considerable individual variability in the number of LC cells observed across the brainstem (German et al., 1988; Manaye et al., 1995). Linking this variability to cognitive function and dysfunction has been difficult in humans because of the small size of the LC relative to the gross resolution of typical imaging protocols.

Several imaging studies implicate the LC in complex cognitive processing and emotion in normal adults (Coull et al., 1999; Labus et al., 2008; Liddell et al., 2005; Sterpenich et al., 2006; Sturm et al., 1999; Tracy et al., 2000), and in the pathophysiology of neurodegenerative and neurodevelopmental disorders (Moore et al., 2008; Remy et al., 2005). However, these results are difficult to validate and replicate because of a lack of information about LC normative position in the standard space most commonly employed in neuroimaging studies. While post-mortem histology-based atlases describing the LC exist (e.g., Duvernoy, 1995), a map of the LC in standard neuroimaging space would provide a means to validate results from these and similar studies, and provide a tool for testing hypotheses about the functional connectivity of the LC with attention-related regions.

High resolution brainstem imaging has recently been used to visualize the LC using a T1-weighted Turbo Spin Echo (T1-TSE) imaging protocol (Sasaki et al., 2006). The T1-TSE sequence allows identification of the LC by exploiting the presence of neuromelanin, a pigment that is produced in noradrenergic neurons (Zecca et al., 2003; Zucca et al., 2006). LC neuromelanin exhibits ferrous properties in the presence of other metals found in the brainstem, such as iron and copper (Enochs et al., 1989; Enochs et al., 1997), therefore providing a unique opportunity to produce an *in vivo* map of the LC that could be

* Corresponding author. Fax: +1 843 792 7736.
E-mail addresses: keren@musc.edu (N.I. Keren), eckert@musc.edu (M.A. Eckert).

1053-8119/$ – see front matter © 2009 Elsevier Inc. All rights reserved.
doi:10.1016/j.neuroimage.2009.06.012

used in imaging studies. Here we describe the development of an empirically derived map of the human LC in a normalized coordinate space that is typically used in neuroimaging studies. To validate our map, we demonstrate that the likelihood of observing LC signal across the brainstem is tightly linked to previously reported histological findings of LC cell density across the same brainstem levels.

Materials and methods

Participants

Forty-four healthy right-handed volunteers [$n=28$ females, $n=16$ males, age range: 19–79, mean age = 48.66 ($\pm$20.40), mean years of education = 16.44 ($\pm$2.39)] were recruited from the Charleston, S.C. community. A semi-structured interview was used to screen for exclusion criteria, including history of head trauma with loss of consciousness, seizures, neurological or language disorders, and chronic or recent use of central nervous system acting medications. Participants' socioeconomic status (SES) [mean SES = 51.35 ($\pm$9.71)] was assessed to characterize the demographic profile of our sample using a revised version of the Hollingshead 4-factor index (Hollingshead, 1975). All participants were administered the Mini Mental State Examination (MMSE) (Folstein et al., 1983) to screen for declines in global cognitive function [mean score = 29.55 ($\pm$0.79)]. Each subject used their right hand for writing and exhibited an Edinburgh Handedness Inventory score of at least 65 [mean score = 91.27 ($\pm$10.47)] (Oldfield, 1971). The Medical University of South Carolina (MUSC) Institutional Review Board approved this study and written informed consent was obtained from all volunteers prior to participation.

Image acquisition

Magnetic resonance imaging (MRI) was performed on a Phillips 3-Tesla Intera scanner using a SENSE 8-channel parallel head coil (Phillips Medical Systems, Bothell WA, USA). High resolution images of the LC were acquired using T1-TSE structural scans with the following parameters: scan resolution of 512 mm $\times$ 320 mm, in-plane resolution of 0.4 mm $\times$ 0.4 mm, field of view (FOV) = 220 mm $\times$ 175.31 mm $\times$ 30 mm, echo time (TE) = 14 ms, repetition time (TR) = 600 ms, flip angle = 90°. Each T1-TSE scan consisted of ten 3 mm-thick axial sections with no gaps. For each participant, we used the mid-sagittal slice of a survey scan to align the LC acquisition volume. Images were acquired perpendicular to the plane of the brainstem, or as cross-sections of the brainstem from the top to the base of the pons. The duration of the T1-TSE scan was approximately 11 min.

Image pre-processing

The following pre-processing steps were taken before normalizing the individual brainstem scans into standard Montreal Neurological Institute (MNI) space. The images were corrected for spatial intensity variations due to field inhomogeneities using FSL 4.0 FAST (Zhang et al., 2001; http://www.fmrib.ox.ac.uk/fsl/) (Fig. 1a). To improve co-registration and normalization, the tissue surrounding the brainstem was cropped away using MRIcro (Rorden and Brett, 2000; http://www.mricro.com) (Fig. 1b). Brainstem cropping boundaries were determined on axial slices, browsing superiorly from the most ventral slice. The ventral boundary was set at the last axial slice on which the nodulus of the cerebellum was visible in the fourth ventricle. The dorsal boundary was set on the most superior slice on which the crural cistern, or gap between the cerebral peduncle and uncal gyrus, was visible. These boundaries were consistently observed in all our participants, and encompassed brainstem regions that include previously reported LC neurons (Chan-Palay and Asan, 1989b; German et al., 1988). Grand mean scaling was applied to the cropped brainstem images using SPM5 (Wellcome Department of Cognitive Neurology, University College, London, UK; http://www.fil.ion.ucl.ac.uk/spm/) to standardize the range of voxel intensity distribution across images. Each brainstem image was aligned in the axial and coronal planes of section and the origin of each image was set to a stable anatomical boundary. Specifically, the origin was defined as the midline at the boundary of the anterior wall of the fourth ventricle, on the slice at which the anterior medullary velum appeared to separate from the brainstem on the axial plane of section.

The brainstem images were normalized into MNI space using a 3-step procedure. 1) A study-specific brainstem template was created by normalizing each cropped brainstem image to a binary image representing the average of all the native space cropped brainstem images [(Fig. 1c); SPM5 normalization parameters: 7th degree B-spline, no source and template image smoothing, writing voxel size = 0.4 mm $\times$ 0.4 mm $\times$ 3 mm]. This normalization approach effectively co-registered all the images to the global shape and boundaries of the average brainstem. 2) The normalized images were averaged, and this averaged image was then normalized into MNI space by using the T1 MNI-152 template (0.5 mm iso-voxel), which had been rotated -0.3 rad into the orientation of the cropped brainstems, as a reference image. As shown previously (Napadow et al., 2006), we observed superior normalization by cropping the MNI template to have the same boundaries as the cropped brainstem images. Using an identical approach to Napadow et al. (2006), we produced a study-specific template that has the size and shape of the MNI brainstem while also preserving the variation in local signal intensity of the T1-TSE images that represents brainstem structures such as the LC, superior cerebellar peduncle, medial lemniscus, and medial longitudinal fasciculus (Fig. 1d). 3) The individual native space brainstems were then normalized to the study-specific T1-TSE MNI space brainstem template (Fig. 1e).

LC maximum intensity location and variation

We observed an increase in T1-TSE signal in brainstem sections that correspond to the position of the LC in post-mortem tissue (Fig. 2). Previous studies employing T1-TSE scans have used the contrast ratio of signal intensity between the LC and adjacent pontine tegmentum as a quantitative measure of LC signal intensity (Sasaki et al., 2006; Shibata et al., 2006; Shibata et al., 2008; Shibata et al., 2007). Using this approach for our data we observed, however, that the pontine tegmentum was not a suitable baseline measure because it exhibited a significant age-related decline in signal ($r_{(42)}=-0.40$, $p<0.01$). Moreover, the boundaries of elevated LC T1-TSE signal are amorphous and variable across individuals, making it difficult to reliably delineate the region from surrounding tissue. Therefore, to derive a map of the LC we took an approach that is independent of LC boundary definition or signal intensity thresholding by identifying the coordinate positions of peak T1-TSE signals across the rostral to caudal extent in each individual's brainstem image (Figs. 1e–g).

MRIcro was used to create bilateral spherical regions of interest (ROI) encompassing areas of high voxel intensity adjacent to the fourth ventricle on each 3 mm-thick axial slice, across individuals (Fig. 1e). Each volume was viewed in MRIcro using a 1:5 contrast ratio. Beginning on the axial slice on which LC voxel intensity was most pronounced, separate left and right oval ROIs were created over areas where high intensity voxels were observed. The superior boundary for data collection was at the level of the interpeduncular fossa. In cases where two high intensity clusters were observed in superior slices, ROIs were defined to include only the anterior cluster (the posterior cluster corresponding in location to the trochlear nerve) that was continuous with the high intensity LC cluster in the immediately inferior slice.

For each ROI, voxels were sorted by *Z*-axis coordinate and intensity, and the location of the highest intensity voxel on each axial slice was recorded. The maximum intensity coordinates for each subject were

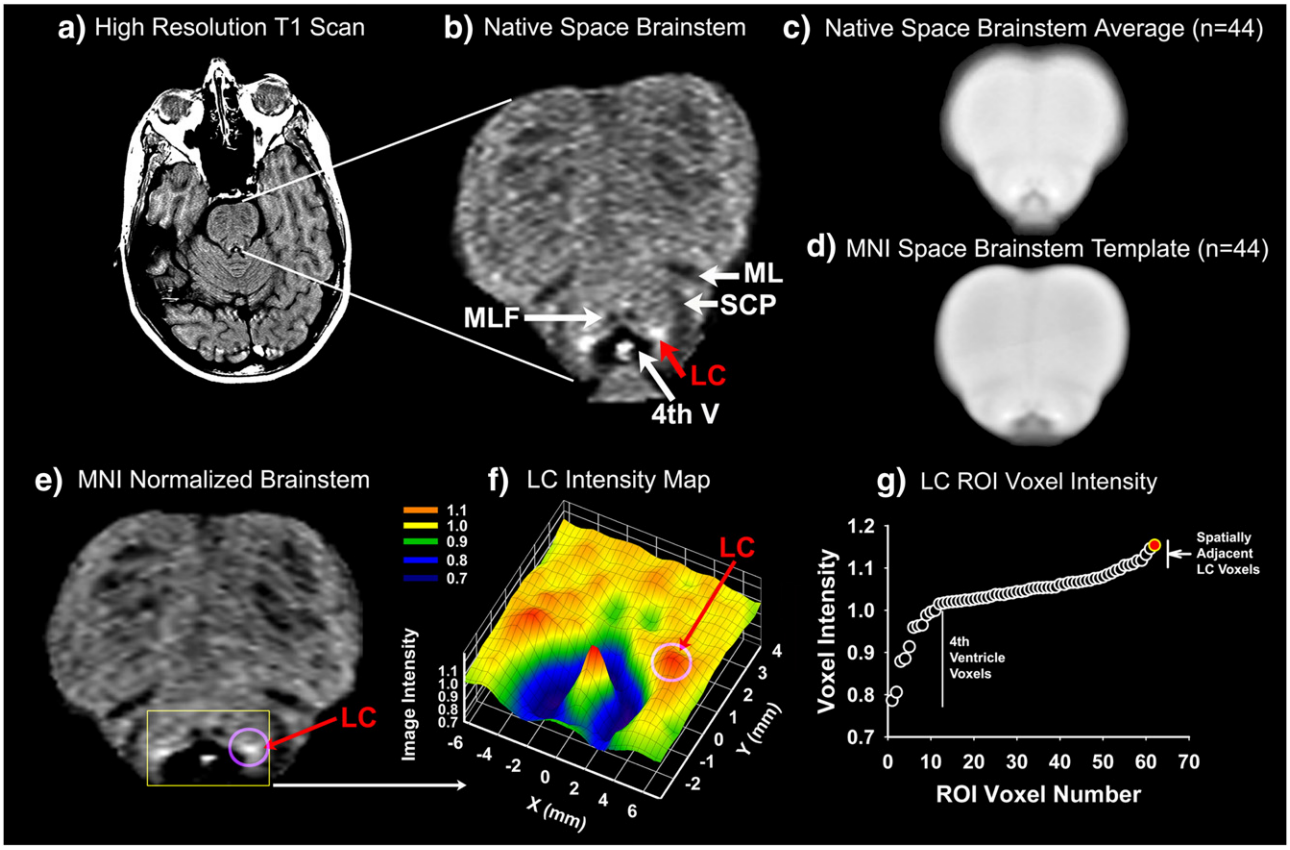

Fig. 1. An overview of the methods used to identify LC coordinates. (a) The high resolution T1-TSE scan was cropped to retain only the brainstem shown in (b), in which the LC (red arrow and text), the superior cerebellar peduncle (SCP), the medial lemniscus (ML), the medial longitudinal fasciculus (MLF), and the fourth ventricle (4th V) can be seen. (c) The 44 brainstem images were realigned and co-registered together to create an average brainstem image. (d) The average brainstem image was then normalized to the MNI template brainstem, which had been cropped from the rest of the MNI brain and rotated −0.3 rad to be aligned with the average brainstem. The original native space brainstem images were normalized to the average MNI-normalized image, shown in (d), which placed each subject's brainstem into the shape and size of the MNI template. (e) The MNI-normalized brainstem of the subject shown in (a) and (b). (f) A signal intensity map of the space surrounding the fourth ventricle [from the yellow square in (e)]. Note the peak signals corresponding to the position of the LC. (g) A plot of the signal intensity of voxels in the area corresponding to the LC [from the red oval shown in (e)]. Note that the highest signal intensity voxels are spatially adjacent voxels that correspond to the position of the LC in post-mortem tissue (see Fig. 2).

plotted, and any left–right disparities in the ventral–dorsal extent of the LC cluster were manually confirmed. An aggregated plot of maximum intensity voxels across subjects was created and spatial outliers were checked by two raters on each axial slice in order to ascertain continuity with adjacent superior and inferior slices. Intra-rater and inter-rater reliability for classification of outlier voxels was $\alpha = 0.97$ and $\alpha = 0.93$, respectively. In order to describe LC location and spatial distribution in standard MNI space, we rotated the coordinates obtained across our sample back into MNI orientation by applying a reverse pitch of 0.3 rad. Each *X,Y,Z* coordinate was then adjusted to reflect the transformation between the native brainstem origin, and standard MNI anterior commissure origin. With the LC maximum intensity voxel coordinates now in standard MNI space and orientation (Fig. 3a), group means and standard deviations (SD) of the left and right LC locations were computed for each axial slice (Table 1).

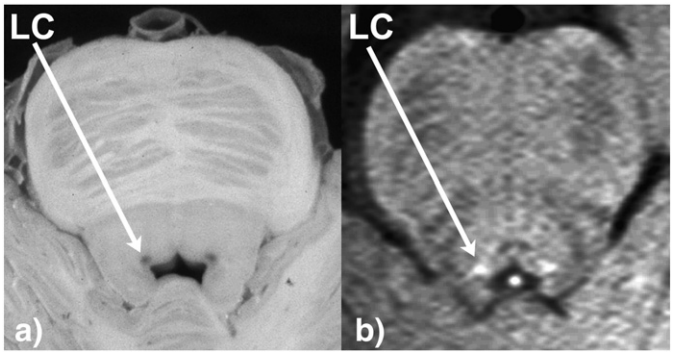

Fig. 2. The human LC (axial view) as seen on (a) post-mortem histological brainstem section, and (b) *in vivo* high resolution (in-plane: 0.4 mm × 0.4 mm) T1-TSE scan. Note the common position of the pigmented signal in post-mortem brainstem slice and elevated signal intensity in the T1-TSE scan adjacent to the fourth ventricle. (The post-mortem image was generously donated by Tanya Ferguson and was adapted from Figs. 4–10 on page 183 of: Nadeau, S., Ferguson, T.S., Valenstein, E., Vierck, C.J., Petruska, J.C., Streit, W.J., Ritz, L.A., 2003. Medical Neuroscience, W.B. Saunders Publishing, Philadelphia.)

LC location probability map

In order to accurately rotate the LC coordinates (group mean) into the original space of the MNI template, the LC ventral–dorsal (*Z*-axis) coordinates were first parcellated from 3 mm image acquisition resolution into 0.5 mm segments corresponding to the template resolution. This step allowed for accurate spatial registration to the 0.5 mm iso-voxel MNI-152 template. The coordinates of mean LC maximum intensity voxel location in standard MNI orientation and space were then used to create an image using a custom Matlab (Mathworks Inc., Sherborn, MA, USA) function. To characterize variation in location of the LC signal across individuals, we created separate maps representing the spatial distribution of LC maximum intensity voxel at 1, and 2 SD from the mean. The probability maps were created by separately smoothing in the *X* and *Y* dimensions of each in-plane 0.5 mm section of our mean location image. Smoothing was applied using a Full-Width Half-Maximum filter with kernel parameters being the standard deviation values of LC maximum

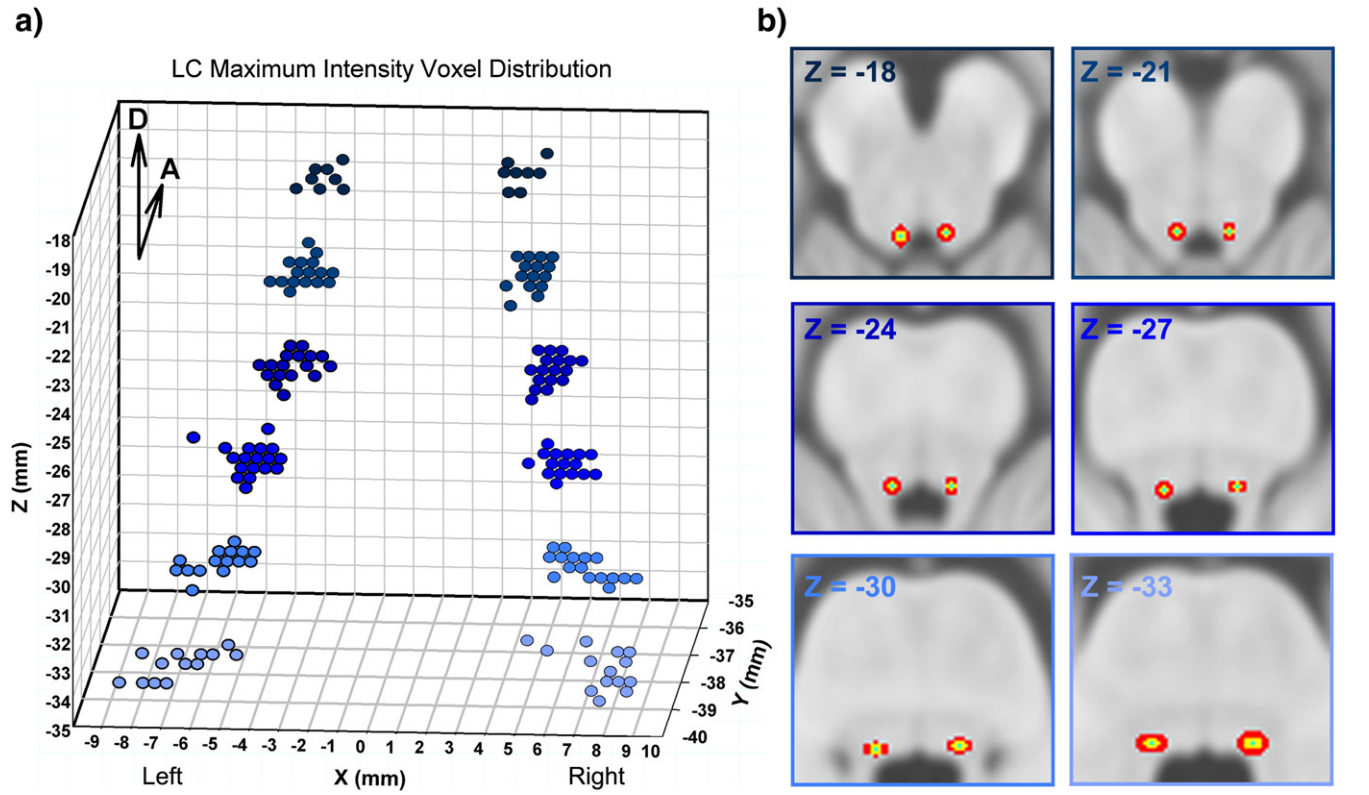

Fig. 3. Variance maps of the human LC. (a) Distribution of the peak LC signal across each brainstem section in *X,Y,Z* MNI space. Note that the variance increases in lower sections (light blue), where fewer subjects exhibited a reliably observable LC signal. A and D arrows indicate anterior and dorsal directions, respectively. [Number of subjects with observed LC signal in each axial section (L/R): 11/11, 32/35, 42/42, 42/41, 34/32, 14/17, for MNI $Z = -18, -21, -24, -27, -30, -33$, respectively.] (b) One (yellow) and two (red) standard deviation maps of the position of the LC on each axial brainstem section of the MNI template. The teal area indicates the mean position of the LC across subjects. The six axial MRI slices correspond to the six *Z*-coordinates represented in (a).

intensity voxel distribution obtained from the corresponding axial slice (Fig. 3a). The individually smoothed voxels were then recombined to create a single image representing the mean, 1 SD, and 2 SD spatial variance of the peak LC signal (Fig. 3b).

Validation with post-mortem LC cell counts

To validate that the high T1-TSE signal represents LC cells, we examined the association between the frequency of an LC signal across each brainstem section and the percent of LC cells that have been reported for the corresponding sections in a post-mortem histological study in humans (German et al., 1988). German et al. (1988) describe LC cell counts from 17 to 22 sections obtained at 0.8 mm gaps along the rostracaudal extent of the nucleus in 4 post-mortem brains. Both the histological sections and our T1-TSE scans were oriented perpendicular to the long axis of the brainstem, allowing us to use the frenulum of the inferior colliculus as a common anatomical reference. We extracted the number of LC cells from five histological sections on Fig. 6 of German et al. (1988), which corresponded in rostracaudal position to our T1-TSE brainstem images. Intra-rater and inter-rater reliability for the estimated left and right cell counts across the 5 sections and 4 subjects was $\alpha = 0.95$ and $\alpha = 0.95$, respectively. The number of cells for each left and right LC was then expressed as a percentage of the total number of LC cells across the brainstem. To limit error in extrapolating the number of cells from Fig. 6 in German et al. (1988), the percentage of left and right LC cells from each section were averaged together and then averaged across all 4 post-mortem cases. We were then able to determine the extent to which the percentage of LC cells on each post-mortem section, related to the frequency of observing an LC signal on corresponding sections of the T1-TSE images.

Statistical analyses

Means and standard deviations were calculated to describe the spatial location and distribution of observed LC maximum intensity

Table 1
LC spatial location and distribution.

MNI *Z*-axis position (mm)	Number (frequency) of cases observed[a]		LC mean signal location (mm) and distribution (±SD) in MNI space			
	Left (%)	Right (%)	Left		Right	
			X	*Y*	*X*	*Y*
−18	11 (25)	11 (25)	−2.5 (±0.5)	−36.3 (±0.6)	4.1 (±0.4)	−36.2 (±0.5)
−21	32 (73)	35 (80)	−3.1 (±0.4)	−36.7 (±0.5)	4.6 (±0.4)	−36.6 (±0.5)
−24	42 (95)	42 (80)	−3.7 (±0.5)	−37.0 (±0.4)	5.2 (±0.4)	−36.9 (±0.5)
−27	42 (95)	41 (95)	−4.7 (±0.6)	−37.3 (±0.4)	5.8 (±0.5)	−37.2 (±0.4)
−30	34 (77)	32 (93)	−5.5 (±0.7)	−37.8 (±0.4)	6.4 (±0.8)	−37.7 (±0.4)
−33	14 (32)	17 (39)	−6.9 (±1.0)	−38.6 (±0.6)	7.6 (±1.1)	−38.5 (±0.7)

[a] Total sample: $n = 44$.

voxel coordinates. Pearson correlation was performed to determine the extent to which the frequency of an LC measure was associated with the percentage of post-mortem LC cells on corresponding brainstem sections. Pearson and Spearman rho correlations were performed to examine the extent to which demographic factors influenced the spatial position of the LC.

Results

MNI location of the LC

An increase in T1-TSE signal intensity was observed in brainstem sections that correspond to the position of the LC in post-mortem tissue (Fig. 2). LC signal was consistently observed in rostral to caudal sections between the inferior aspect of the red nucleus (upper limit of the image acquisition) and the origin of the superior cerebellar peduncle [MNI $Z=-18$ to -33; (Figs. 3a, b)]. Fig. 3b presents a spatial variance map for the location of the peak LC signal (mean position, 1 SD and 2 SD in the *X*–*Y* plane). The mean LC location coordinates in the *X*–*Y* plane along with observed signal distribution along the *Z*-axis are presented in Table 1.

Association with post-mortem histology

We examined the extent to which the frequency of LC signal across subjects at each brainstem level was associated with the number of cells that have been reported at the same brainstem levels in 4 post-mortem human brains [Fig. 6 in German et al. (1988)]. A higher percentage of subjects exhibited LC signal at the level of the medial longitudinal fasciculus (MNI $Z=-24$ and -27), in comparison to the most rostral and caudal levels (Table 1). This elevated frequency of high intensity signal corresponded with the location of greatest LC neuron density as reported from post-mortem tissue (German et al., 1988). Indeed, variation in LC signal was significantly correlated with the percentage of cell counts across the left and right LC for the 5 common brainstem levels [$r=0.90$; (Fig. 4)], thereby providing evidence that T1-TSE LC signal is related to the number of LC cells.

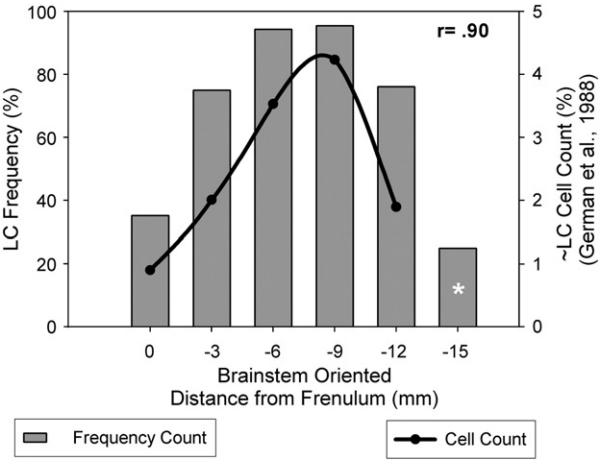

Fig. 4. The association between T1-TSE LC signal observed across our sample and LC cell counts previously reported in post-mortem histology sections (German et al., 1988). The *X*-axis represents the distance from the frenulum of the inferior colliculus, which was used as an anatomical landmark for identifying common brainstem sections in both studies. The left *Y*-axis represents the percent of subjects in which a T1-TSE LC signal was detected. The right *Y*-axis represents the percent of total LC cells observed along the long axis of the brainstem in German et al. (1988). The bars represent the frequency of observed T1-TSE LC signal across our sample ($n=44$), while the black line represents the percentage of LC cells reported on corresponding histology sections. The section corresponding to our most caudal slice (-15 mm from frenulum) was not included in the post-mortem LC study (white asterisk). Note the very strong correspondence between the two measures ($r=0.90$), providing evidence that the likelihood of observing an LC signal is related to the density of LC cells.

Individual variation in LC signal

Based on previous findings of age-related increases in LC neuromelanin (Zecca et al., 2004; Zecca et al., 2003; Zucca et al., 2006) and T1-TSE signal (Shibata et al., 2006), Spearman rho correlations were performed to determine the extent to which age influenced the likelihood of observing an LC signal in rostral to caudal brainstem sections. Older adults were more likely to exhibit an LC signal in the most caudal sections (left MNI $Z=-30$: $r_{(43)}=0.34$, $p<0.05$; right MNI $Z=-33$: $r_{(43)}=0.34$, $p<0.05$), while younger adults were more likely to exhibit an LC signal in the most rostral sections (left MNI $Z=-18$: $r_{(43)}=0.27$, $p<0.10$; right MNI $Z=-21$: $r_{(43)}=-0.33$, $p<0.05$). Increasing age was also significantly correlated with more medial left (MNI $Z=-18$: $r_{(10)}=0.77$, $p<0.05$; MNI $Z=-24$: $r_{(41)}=0.31$, $p<0.05$) and right (MNI $Z=-24$: $r_{(41)}=-0.31$, $p<0.05$) peak LC signal. On section $Z=-24$, where there was the highest concentration of subjects with an LC signal, the LC shifted medially at a rate of 0.06 mm and 0.08 mm respectively for each decade between 20 and 80 years of age. The only significant rostral to caudal dimension that exhibited a significant correlation with age was on section MNI $Z=-27$ in which older adults were more likely to exhibit a more posterior LC ($r_{(41)}=-0.43$, $p<0.05$). There were no other demographic factors that were significantly associated with the LC measurements after correcting for multiple comparisons. Supplemental Table 1 presents all of the uncorrected correlations between age, handedness, and gender for each left and right mean LC position.

Discussion

We have taken advantage of the elevated T1-TSE signal that has been attributed to neuromelanin in the LC (Sasaki et al., 2006) to develop a spatial map of the human LC in 44 adults ranging in age from 19 to 79 years. The development of this map, which has been oriented into a standard coordinate space that is often used in neuroimaging research, is important because: 1) it is the first *in vivo* anatomical map of the human LC; 2) it shows that T1-TSE LC signal is related to the number of LC cells observed in post-mortem material; 3) the spatial variance map can be used as an anatomical reference for determining the extent to which a particular brainstem finding falls within the LC; and 4) it can be used to test hypotheses about the functional connectivity of the LC with cortical and sub-cortical systems. T1-TSE LC signal was observed from the level of the oculomotor nerve to the trigeminal nerve. These results are consistent with the rostral to caudal range in which LC cells are identified in histological sections (Chan-Palay and Asan, 1989b; German et al., 1988; Manaye et al., 1995), with the exception of more rostral sections approaching the tectum that were not included during image acquisition. We investigated whether the frequency of observing an LC signal would relate to the density of the LC cells at the corresponding histological sections. By examining the percentage of LC cells reported in a post-mortem study (German et al., 1988) and using a common anatomical landmark, we were able to determine that the frequency of an observable LC signal was indeed tightly correlated with the percentage of cells across brainstem sections that were consistent between the two studies. These results provide convincing evidence that the T1-TSE LC signal is related to the number of LC cells and thereby provides indirect validation that this signal is generated by LC cells.

The fact that we observed T1-TSE LC signal in sections corresponding to the greatest concentration of LC cells is consistent with the notion that LC signal on T1-TSE scans is influenced by the ferrous neuromelanin metabolites within LC neurons (Sasaki et al., 2006). Paramagnetic T1 effects are observed when neuromelanin is combined with iron and copper (Enochs et al., 1989; Enochs et al., 1997). Iron and copper are present with neuromelanin in LC cells and while

the content of iron remains constant across life, there is an increase in neuromelanin and copper with age (Zecca et al., 2004; Zucca et al., 2006). Age-related increases in neuromelanin have been attributed to its relative slow rate of metabolism in neurons (Zecca et al., 2004; Zecca et al., 2003).

Post-mortem observations of the total number of cells and the distribution of the cells indicate that the LC is largely symmetrical in size and position (Chan-Palay and Asan, 1989a,b; German et al., 1988; Ohm et al., 1997). Our results are consistent with these post-mortem studies, but are not perfectly symmetrical in peak location or in the variance of the peak location. A similar degree of left to right variation in LC cell distribution has been reported among post-mortem brains [Fig. 9 in German et al. (1988)]. Consistent with post-mortem evidence for age-related increases in neuromelanin (Zecca et al., 2004; Zucca et al., 2006) older adults in this study were more likely to exhibit observable LC signal in the most caudal brainstem sections. The inclusion of subjects from across the adult lifespan yielded a map that is representative of the general adult population, but also increased the spatial extent of the map because of the age-related factors that positively influenced identification of the LC.

In addition to age, one other explanation for individual spatial variability of the T1-TSE LC signal is the method by which each LC coordinate was defined. Selecting the maximal LC signal, which should reflect the greatest density of LC cells within a section (Fig. 4), was chosen for its superior reliability compared to automated segmentation or manual tracing of the LC signal. Automated or manual segmentation of the LC is difficult because of the amorphous structure of the LC and varying signal intensity across subjects. Future work involving quantitative T1-TSE scans may provide a more detailed map of LC spatial distribution. Nonetheless, creating a map based on the 1 and 2 SD of spatial variation should represent the core of the LC given its spatial extent of ~1–2 mm in the axial plane (Chan-Palay and Asan, 1989b; German et al., 1988; Hoogendijk et al., 1995). As Fig. 3a demonstrates, there is limited variation in the medial to lateral and anterior to posterior extent of the individual LC coordinates, which is further demonstrated in Fig. 3b by the low degree of spatial variation in the 2 SD boundary of the LC map (mean extent of 2 SD map: $X = 2.96$ mm, $Y = 2.71$ mm).

When using imaging methodology to characterize the *in vivo* location of small brainstem structures it is important to consider the potential effect of brain motion associated with the cardiac cycle and cerebrospinal fluid flow dynamics on accurate spatial localization. Animal studies (for example, Britt and Rossi, 1982) as well as human imaging studies (Enzmann and Pelc, 1992; Feinberg and Mark, 1987; Greitz et al., 1992; Poncelet et al., 1992; Soellinger et al., 2007) indicate that peak displacement and movement velocity of brain tissue occur at the brainstem along the rostral–caudal axis. However, at its maximum, the spatial displacement of brainstem tissue is small relative to the resolution in which our images were acquired (0.4 mm × 0.4 mm × 3.0 mm). For example, a motion sensitive MR pulse sequence was used to demonstrate that the average peak displacement along the rostral–caudal axis in the upper brainstem was 0.160 (±0.020) mm (Enzmann and Pelc, 1992). More recently a different motion sensitive sequence was used to demonstrate an average peak displacement of 0.184 (±0.021) mm along the rostral–caudal axis of the brainstem (Soellinger et al., 2007), confirming previous observations. Given these results, it seems unlikely that pulsatile brain motion would affect the spatial accuracy of our probability map. Furthermore, throughout the brain, pulsatile displacement in the left–right and anterior–posterior directions (*X*-axis and *Y*-axis, respectively) is even smaller than that observed on the rostral–caudal axis (Soellinger et al., 2009) and is difficult to measure (Enzmann and Pelc, 1992) suggesting that the motion on the *X*–*Y* plane is within the error expressed in our location probability measurements [smallest 1 SD spatial extent = 0.4 mm (see Table 1)].

A major methodological challenge that was successfully addressed in this study was the normalization of each brainstem image into standard MNI coordinate space. Guided by previous work on normalizing brainstem images (Napadow et al., 2006), we used a mask to limit estimation of the normalization parameters to rostral–caudal brainstem sections. This approach minimized realignment and transformation errors that result in sub-optimal co-registration of the brainstem when using whole-brain normalization (Napadow et al., 2006). In this study, we took an additional step to obtain the best possible normalization by creating a study-specific brainstem template that had been co-registered with the MNI template. This approach ensured that the shape and size of the MNI brainstem template, as well as the signal variations present within the brainstem of the T1-TSE images contributed to the normalization of the LC.

The placement of the LC map into MNI space creates a variety of potential applications. For example, strong inferences have been made based on low-resolution brainstem activation results that appear to fall within the space of the LC. We used the 2 SD map to determine the extent to which LC activity reported in previous functional imaging studies could be confirmed as falling within the space of the LC. Twelve studies were found in which 28 coordinates were associated with the LC [7 functional MRI (fMRI) studies (Berman et al., 2008; Liddell et al., 2005; Minzenberg et al., 2008; Raizada and Poldrack, 2007; Sterpenich et al., 2006; Tracy et al., 2000; Vandewalle et al., 2007), 5 positron emission tomography (PET) studies (Coull et al., 1999; Labus et al., 2008; Moore et al., 2008; Remy et al., 2005; Sturm et al., 1999). Coordinates reported in Talairach space were first converted to MNI coordinates using GingerALE (Laird et al., 2005; http://brainmap.org/ale/)]. Four of these coordinates (14%) were within or immediately adjacent (<1 mm) to the 2 SD boundary of our LC map. While the frequency of overlap with our template is low, we only examined the peak voxel location rather than the extent of activations [the average extent of reported LC clusters was 162.71 (±174.11) voxels (available for $n = 14$ of the coordinates)]. Thus, peak coordinates falling outside of the LC map may have had a cluster extent that overlapped with the LC map. An additional consideration is that the studies we reviewed employed whole-brain normalization, which may account for spatial differences in reported locations as previously demonstrated (Diedrichsen, 2006; Napadow et al., 2006). Nonetheless, the low frequency of concordance between locations of brainstem activation and the LC map highlights the importance of having an anatomical reference for verifying the location of brainstem findings. Furthermore, we encourage groups interested in using our LC map, to utilize brainstem-specific normalization when examining brainstem activity and morphology across participants. In order to facilitate future use of the LC map produced by our study, two binary templates representing the 1 SD and 2 SD extents of LC spatial distribution (see Fig. 3b) are freely available for download and use by the neuroimaging community (http://www.eckertlab.org/LC).

LC function is critical to understanding normal attention, aging, psychiatric disorders, neurodegenerative disorders, and pharmaceutical treatments. With the careful normalization of brainstem images, as well as controls for physiological nose, the LC map presented here can be used in functional imaging studies to: 1) collect timeseries of LC activity and test hypotheses about the interaction of the LC with cortical areas across tasks that tap into domains of attention (Aston-Jones et al., 2000; Corbetta et al., 2008); 2) evaluate functional changes in LC-attention systems that occur during development or in neurodegenerative disorders involving LC disruptions such as Alzheimer's and Parkinson's disease (Chan-Palay and Asan, 1989a; German et al., 1992; Hoogendijk et al., 1995); and 3) as a biomarker for the efficacy of attention-related pharmaceutical treatments.

Acknowledgments

We would like to thank the participants of this study, the National Institute on Deafness and other Communication Disorders (P50

DC00422), and the MUSC Center for Advanced Imaging Research. We would also like to thank Gary Aston-Jones for his comments on the manuscript. This investigation was conducted in a facility constructed with support from Research Facilities Improvement Program (C06 RR14516) from the National Center for Research Resources, National Institutes of Health. This research was conducted while Mark Eckert was a research grant recipient of the American Federation for Aging Research.

Appendix A. Supplementary data

Supplementary data associated with this article can be found, in the online version, at doi:10.1016/j.neuroimage.2009.06.012.

References

Aston-Jones, G., Rajkowski, J., Cohen, J., 2000. Locus coeruleus and regulation of behavioral flexibility and attention. Prog. Brain Res. 126, 165–182.
Berman, S.M., Nailboff, B.D., Suyenobu, B., Labus, J.S., Stains, J., Ohning, G., Kilpatrick, L., Bueller, J.A., Ruby, K., Jarcho, J., Mayer, E.A., 2008. Reduced brainstem inhibition during anticipated pelvic visceral pain correlates with enhanced brain response to the visceral stimulus in women with irritable bowel syndrome. J. Neurosci. 28, 349–359.
Bouret, S., Sara, S.J., 2005. Network reset: a simplified overarching theory of locus coeruleus noradrenaline function. Trends Neurosci. 28, 574–582.
Britt, R.H., Rossi, G.T., 1982. Quantitative analysis of methods for reducing physiological brain pulsations. J. Neurosci. Methods 6, 219–229.
Chan-Palay, V., Asan, E., 1989a. Alterations in catecholamine neurons of the locus coeruleus in senile dementia of the Alzheimer type and in Parkinson's disease with and without dementia and depression. J. Comp. Neurol. 287, 373–392.
Chan-Palay, V., Asan, E., 1989b. Quantitation of catecholamine neurons in the locus coeruleus in human brains of normal young and older adults and in depression. J. Comp. Neurol. 287, 357–372.
Corbetta, M., Patel, G., Shulman, G.L., 2008. The reorienting system of the human brain: from environment to theory of mind. Neuron 58, 306–324.
Coull, J.T., Buchel, C., Friston, K.J., Frith, C.D., 1999. Noradrenergically mediated plasticity in a human attentional neuronal network. NeuroImage 10, 705–715.
D'Ardenne, K., McClure, S.M., Nystrom, L.E., Cohen, J.D., 2008. BOLD responses reflecting dopaminergic signals in the human ventral tegmental area. Science 319, 1264–1267.
Diedrichsen, J., 2006. A spatially unbiased atlas template of the human cerebellum. NeuroImage 33, 127–138.
Duvernoy, H.M., 1995. The Human Brain Stem and Cerebellum: Surface, Structure, Vascularization, and Three-dimensional Sectional Anatomy with MRI. Springer-Verlag, Wien; New York.
Enochs, W.S., Hyslop, W.B., Bennett, H.F., Brown III, R.D., Koenig, S.H., Swartz, H.M., 1989. Sources of the increased longitudinal relaxation rates observed in melanotic melanoma. An in vitro study of synthetic melanins. Invest. Radiol. 24, 794–804.
Enochs, W.S., Petherick, P., Bogdanova, A., Mohr, U., Weissleder, R., 1997. Paramagnetic metal scavenging by melanin: MR imaging. Radiology 204, 417–423.
Enzmann, D.R., Pelc, N.J., 1992. Brain motion: measurement with phase-contrast MR imaging. Radiology 185, 653–660.
Feinberg, D.A., Mark, A.S., 1987. Human brain motion and cerebrospinal fluid circulation demonstrated with MR velocity imaging. Radiology 163, 793–799.
Folstein, M.F., Robins, L.N., Helzer, J.E., 1983. The Mini-Mental State Examination. Arch. Gen. Psychiatry 40, 812.
German, D.C., Walker, B.S., Manaye, K., Smith, W.K., Woodward, D.J., North, A.J., 1988. The human locus coeruleus: computer reconstruction of cellular distribution. J. Neurosci. 8, 1776–1788.
German, D.C., Manaye, K.F., White III, C.L., Woodward, D.J., McIntire, D.D., Smith, W.K., Kalaria, R.N., Mann, D.M., 1992. Disease-specific patterns of locus coeruleus cell loss. Ann. Neurol. 32, 667–676.
Greitz, D., Wirestam, R., Franck, A., Nordell, B., Thomsen, C., Ståhlberg, F., 1992. Pulsatile brain movement and associated hydrodynamics studied by magnetic resonance phase imaging. Neuroradiology 34, 370–380.
Hollingshead, A.B., 1975. Four Factor Index of Social Status. Yale University, New Haven, CT.
Hoogendijk, W.J., Pool, C.W., Troost, D., van Zwieten, E., Swaab, D.F., 1995. Image analyser-assisted morphometry of the locus coeruleus in Alzheimer's disease, Parkinson's disease and amyotrophic lateral sclerosis. Brain 118 (Pt 1), 131–143.
Labus, J.S., Naliboff, B.N., Fallon, J., Berman, S.M., Suyenobu, B., Bueller, J.A., Mandelkern, M., Mayer, E.A., 2008. Sex differences in brain activity during aversive visceral stimulation and its expectation in patients with chronic abdominal pain: a network analysis. NeuroImage 41, 1032–1043.
Laird, A.R., Fox, P.M., Price, C.J., Glahn, D.C., Uecker, A.M., Lancaster, J.L., Turkeltaub, P.E., Kochunov, P., Fox, P.T., 2005. ALE meta-analysis: controlling the false discovery rate and performing statistical contrasts. Hum. Brain Mapp. 25, 155–164.
Liddell, B.J., Brown, K.J., Kemp, A.H., Barton, M.J., Das, P., Peduto, A., Gordon, E., Williams, L.M., 2005. A direct brainstem-amygdala-cortical 'alarm' system for subliminal signals of fear. NeuroImage 24, 235–243.
Manaye, K.F., McIntire, D.D., Mann, D.M., German, D.C., 1995. Locus coeruleus cell loss in the aging human brain: a non-random process. J. Comp. Neurol. 358, 79–87.
Minzenberg, M.J., Watrous, A.J., Yoon, J.H., Ursu, S., Carter, C.S., 2008. Modafinil shifts human locus coeruleus to low-tonic, high-phasic activity during functional MRI. Science 322, 1700–1702.
Mohanty, A., Gitelman, D.R., Small, D.M., Mesulam, M.M., 2008. The spatial attention network interacts with limbic and monoaminergic systems to modulate motivation-induced attention shifts. Cereb. Cortex 18, 2604–2613.
Moore, R.Y., Whone, A.L., Brooks, D.J., 2008. Extrastriatal monoamine neuron function in Parkinson's disease: an 18F-dopa PET study. Neurobiol. Dis. 29, 381–390.
Morecraft, R.J., Geula, C., Mesulam, M.M., 1992. Cytoarchitecture and neural afferents of orbitofrontal cortex in the brain of the monkey. J. Comp. Neurol. 323, 341–358.
Morrison, J.H., Foote, S.L., O'Connor, D., Bloom, F.E., 1982. Laminar, tangential and regional organization of the noradrenergic innervation of monkey cortex: dopamine-beta-hydroxylase immunohistochemistry. Brain Res. Bull. 9, 309–319.
Morrison, J.H., Foote, S.L., 1986. Noradrenergic and serotoninergic innervation of cortical, thalamic, and tectal visual structures in Old and New World monkeys. J. Comp. Neurol. 243, 117–138.
Napadow, V., Dhond, R., Kennedy, D., Hui, K.K., Makris, N., 2006. Automated brainstem co-registration (ABC) for MRI. NeuroImage 32, 1113–1119.
Ohm, T.G., Busch, C., Bohl, J., 1997. Unbiased estimation of neuronal numbers in the human nucleus coeruleus during aging. Neurobiol. Aging 18, 393–399.
Oldfield, R.C., 1971. The assessment and analysis of handedness: the Edinburgh inventory. Neuropsychologia 9, 97–113.
Poncelet, B.P., Wedeen, V.J., Weisskoff, R.M., Cohen, M.S., 1992. Brain parenchyma motion: measurement with cine echo-planar MR imaging. Radiology 185, 645–651.
Porrino, L.J., Goldman-Rakic, P.S., 1982. Brainstem innervation of prefrontal and anterior cingulate cortex in the rhesus monkey revealed by retrograde transport of HRP. J. Comp. Neurol. 205, 63–76.
Posner, M. (Ed.), 2004. Cognitive Neuroscience of Attention. InGuilford Press, New-York.
Raizada, R.D., Poldrack, R.A., 2007. Challenge-driven attention: interacting frontal and brainstem systems. Front. Hum. Neurosci. 1, 1–6.
Remy, P., Doder, M., Lees, A., Turjanski, N., Brooks, D., 2005. Depression in Parkinson's disease: loss of dopamine and noradrenaline innervation in the limbic system. Brain 128, 1314–1322.
Rorden, C., Brett, M., 2000. Stereotaxic display of brain lesions. Behav. Neurol. 12, 191–200.
Sasaki, M., Shibata, E., Tohyama, K., Takahashi, J., Otsuka, K., Tsuchiya, K., Takahashi, S., Ehara, S., Terayama, Y., Sakai, A., 2006. Neuromelanin magnetic resonance imaging of locus ceruleus and substantia nigra in Parkinson's disease. NeuroReport 17, 1215–1218.
Shea-Brown, E., Gilzenrat, M.S., Cohen, J.D., 2008. Optimization of decision making in multilayer networks: the role of locus coeruleus. Neural. Comput. 20, 2863–2894.
Shibata, E., Sasaki, M., Tohyama, K., Kanbara, Y., Otsuka, K., Ehara, S., Sakai, A., 2006. Age-related changes in locus ceruleus on neuromelanin magnetic resonance imaging at 3 Tesla. Magn. Reson. Med. Sci. 5, 197–200.
Shibata, E., Sasaki, M., Tohyama, K., Otsuka, K., Endoh, J., Terayama, Y., Sakai, A., 2008. Use of neuromelanin-sensitive MRI to distinguish schizophrenic and depressive patients and healthy individuals based on signal alterations in the substantia nigra and locus ceruleus. Biol. Psychiatry 64, 401–406.
Shibata, E., Sasaki, M., Tohyama, K., Otsuka, K., Sakai, A., 2007. Reduced signal of locus ceruleus in depression in quantitative neuromelanin magnetic resonance imaging. NeuroReport 18, 415–418.
Soellinger, M., Ryf, S., Boesiger, P., Kozerke, S., 2007. Assessment of human brain motion using CSPAMM. J. Magn. Reson. Imaging 25, 709–714.
Soellinger, M., Rutz, A.K., Koezrke, S., Boesiger, P., 2009. 3D Cine displacement-encoded MRI of pulsatile brain motion. Magn. Reson. Med. 61, 153–162.
Sterpenich, V., D'Argembeau, A., Desseilles, M., Balteau, E., Albouy, G., Vandewalle, G., Degueldre, C., Luxen, A., Collette, F., Maquet, P., 2006. The locus ceruleus is involved in the successful retrieval of emotional memories in humans. J. Neurosci. 26, 7416–7423.
Sturm, W., de Simone, A., Krause, B.J., Specht, K., Hesselmann, V., Radermacher, I., Herzog, H., Tellmann, L., Muller-Gartner, H.W., Willmes, K., 1999. Functional anatomy of intrinsic alertness: evidence for a fronto-parietal-thalamic-brainstem network in the right hemisphere. Neuropsychologia 37, 797–805.
Tracy, J.I., Mohamed, F., Faro, S., Tiver, R., Pinus, A., Bloomer, C., Pyrros, A., Harvan, J., 2000. The effect of autonomic arousal on attentional focus. NeuroReport 11, 4037–4042.
Usher, M., Cohen, J.D., Servan-Schreiber, D., Rajkowski, J., Aston-Jones, G., 1999. The role of locus coeruleus in the regulation of cognitive performance. Science 283, 549–554.
Vandewalle, G., Schmidt, C., Albouy, G., Sterpenich, V., Darsaud, A., Rauchs, G., Berken, P.Y., Balteau, E., Degueldre, C., Luxen, A., Maquet, P., Dijk, D.J., 2007. Brain responses to violet, blue, and green monochromatic light exposures in humans: prominent role of blue light and the brainstem. PLoS ONE 2, e1247.
Zecca, L., Zucca, F.A., Wilms, H., Sulzer, D., 2003. Neuromelanin of the substantia nigra: a neuronal black hole with protective and toxic characteristics. Trends Neurosci. 26, 578–580.
Zecca, L., Stroppolo, A., Gatti, A., Tampellini, D., Toscani, M., Gallorini, M., Giaveri, G., Arosio, P., Santambrogio, P., Fariello, R.G., Karatekin, E., Kleinman, M.H., Turro, N., Hornykiewicz, O., Zucca, F.A., 2004. The role of iron and copper molecules in the neuronal vulnerability of locus coeruleus and substantia nigra during aging. Proc. Natl. Acad. Sci. U. S. A. 101, 9843–9848.
Zhang, Y., Brady, M., Smith, S., 2001. Segmentation of brain MR images through a hidden Markov random field model and the expectation-maximization algorithm. IEEE. Trans. Med. Imag. 20, 45–57.
Zucca, F.A., Bellei, C., Giannelli, S., Terreni, M.R., Gallorini, M., Rizzio, E., Pezzoli, G., Albertini, A., Zecca, L., 2006. Neuromelanin and iron in human locus coeruleus and substantia nigra during aging: consequences for neuronal vulnerability. J. Neural Transm. 113, 757–767.